AD-A187 983   THE INFLUENCE OF SMALL DEFECTS ON TENSILE SPECIMEN   1/1
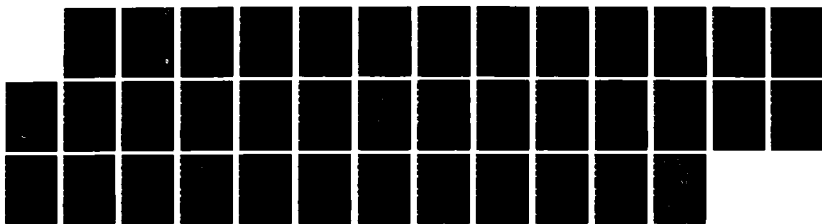   DUCTILITY AND SYMMETRY OF DEFORMATION(U) NAVAL RESEARCH
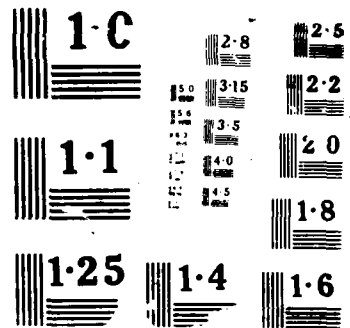   LAB WASHINGTON DC   P MATIC ET AL   04 SEP 87 NRL-MR-5937
UNCLASSIFIED   F/G 20/11   NL

Naval Research Laboratory

AD-A187 983

The Influence of Small Defects on Tensile Specimen Ductility and Symmetry of Deformation

PETER MATIC AND MITCHELL I. JOLLES

Mechanics of Materials Branch
Material Science and Technology Division

September 4, 1987

DTIC
ELECTE
NOV 1 7 1987
E

REPORT DOCUMENTATION PAGE

1a. REPORT SECURITY CLASSIFICATION		1b. RESTRICTIVE MARKINGS	
UNCLASSIFIED			
2a. SECURITY CLASSIFICATION AUTHORITY		3 DISTRIBUTION / AVAILABILITY OF REPORT	
2b. DECLASSIFICATION / DOWNGRADING SCHEDULE		Approved for public release; distribution unlimited.	
4. PERFORMING ORGANIZATION REPORT NUMBER(S)		5. MONITORING ORGANIZATION REPORT NUMBER(S)	
NRL Memorandum Report 5937			

6a. NAME OF PERFORMING ORGANIZATION	6b OFFICE SYMBOL (If applicable)	7a. NAME OF MONITORING ORGANIZATION
Naval Research Laboratory	Code 6382	

6c. ADDRESS (City, State, and ZIP Code)	7b. ADDRESS (City, State, and ZIP Code)
Washington, DC 20375-5000	

8a. NAME OF FUNDING / SPONSORING ORGANIZATION	8b. OFFICE SYMBOL (If applicable)	9. PROCUREMENT INSTRUMENT IDENTIFICATION NUMBER
Office of Naval Research		

8c. ADDRESS (City, State, and ZIP Code)	10. SOURCE OF FUNDING NUMBERS			
	PROGRAM ELEMENT NO.	PROJECT NO.	TASK NO.	WORK UNIT ACCESSION NO
Arlington, VA 22217	61153N22	RR022-01-48		DN480-509

11 TITLE (Include Security Classification)

The Influence of Small Defects on Tensile Specimen Ductility and Symmetry of Deformation

12. PERSONAL AUTHOR(S)
Matic, Peter and Jolles, Mitchell I.

13a. TYPE OF REPORT	13b. TIME COVERED FROM _____ TO _____	14. DATE OF REPORT (Year, Month, Day) 1987 September 4	15. PAGE COUNT 38

16. SUPPLEMENTARY NOTATION

19. ABSTRACT (Continue on reverse if necessary and identify by block number)

The quantitative translation of physical weld quality into structural integrity prediction depends on accurate characterization of weld material behavior in the presence of fabrication defects. The presence of such defects will, however, significantly influence the response of common material test specimens. If the influence of such defects is fully understood, test specimen data may be interpreted in a more meaningful way.

The role of a physically relevant geometric imperfection, in the form of a spherical void defect, on cylindrical tensile specimen response is computationally simulated for HY-100 weld metal. Defect radius and location along the specimen axis are treated as independent parameters. Asymmetry of specimen deformation (in terms of specimen neck location) and specimen ductility (in terms of the reduction of area at failure) are computationally predicted.

(Continues)

20 DISTRIBUTION / AVAILABILITY OF ABSTRACT	21 ABSTRACT SECURITY CLASSIFICATION
[X] UNCLASSIFIED/UNLIMITED [ ] SAME AS RPT [ ] DTIC USERS	UNCLASSIFIED

22a. NAME OF RESPONSIBLE INDIVIDUAL	22b TELEPHONE (Include Area Code)	22c OFFICE SYMBOL
Peter Matic	(202) 767-5215	Code 6382

DD FORM 1473, 84 MAR   83 APR edition may be used until exhausted

All other editions are obsolete.

19. ABSTRACT (Continued)

Results suggest that the neck location does not necessarily coincide with the defect location. Therefore, geometric defects are a sufficient condition for asymmetry of neck location but not a necessary condition for neck formation. In addition, coincidence of the defect and the neck reduces the specimen ductility at failure to a lower bound value which depends on defect size When the defect and neck are separated, the defect free specimen ductility at failure is recovered as an upper bound. The transition between these two ductility values is abrupt, despite the continuum nature of the physical problem. Preliminary implications of these results on the assessment of defect criticality are discussed.

CONTENTS

THE INFLUENCE OF SMALL DEFECTS ON
TENSILE SPECIMEN DUCTILITY AND
SYMMETRY OF DEFORMATION

INTRODUCTION

The quantitative translation of physical weld quality into a form useful for structural integrity prediction of weld systems is a major problem for structural designers and analysts (e.g. Wells (1983)). The wide variety in type and scale of detectable weld defects compounds the problem. Porosity, lack of penetration, lack of fusion and slag inclusion all can be detrimental to weld performance as reviewed by Lundin (1984). Improved characterization of deposited weld material is prerequisite for improved structural integrity prediction of weld systems. As is inevitably the case with all inhomogeneous material systems, whether they are weld systems, fiber reinforced composites, steel reinforced concrete or metal matrix composites, accurate prediction depends on an understanding of the effects the inhomogeneity bring to the global structural response.

Weld metal defects are generally distributed throughout the weld zone. Non-destructive inspection techniques are used to detect and evaluate defects. Welds which contain defects outside acceptable size and shape limits are rejected. Defects below these limits are accepted. Examples of criteria proposed to define allowable limits include work by Harrison (1972a), Harrison (1972b), Boulton (1977) and Lundin (1984). One common aspect of this problem is to undestand how small defects influence the deformation and fracture of simple specimen geometries. This investigation considers spherical void defects in simple cylinderical tensile specimen geometries for HY-100 weld metal. Defect size and location are considered independent parameters for the purpose of computational simulation. Of particular interest are the sensitivity of predicted specimen deformation asymmetry and specimen ductility to defect size and location. These limits are generally obtained through tests of small scale sample welds or selected component geometries. As a result, the limits on the defects are size and geometry dependent and in strict terms serve only as qualitative guidelines for integrity assessment in general.

A comprehensive approach to the quantitative translation of physical weld quality into structural integrity prediction should rely on accurate characterization of weld material behavior in the presence of anticipated defect types and sizes. The accurate characterization of each constituent material's effective continuum behavior removes the issue of size and geometry dependence. This applies equally well to the material behavior gradients present across the heat affected zone of base metal adjacent to the weld m al. It would allow the designer or analyst to incorporate anticipated fabrication quality, or the upper and lower bounds of fabrication quality, into detail design, fabrication design, life cycle prediction and optimization in a manner consistent with existing and future developments in the design process.

MATERIAL CHARACTERIZATION

Cylindrical uniaxial tensile specimens are traditionally used to characterize elastic and inelastic behavior of isotropic materials. The global load-displacement responses of a specimen are normalized to engineering stress-engineering strain and true stress-true strain. Therefore,

$$\bar{\sigma} = \frac{P}{A_0}$$

and

$$\bar{\epsilon} = \frac{L - L_0}{L_0}$$

where $\bar{\sigma}$ is engineering stress, $\bar{\epsilon}$ is engineering strain, P is load, L is specimen deformed length, A_0 is specimen cross sectional area in the undeformed length. Also,

$$\dot{\sigma} = \frac{P}{A}$$

and

$$\dot{\epsilon} = \ln \frac{L}{L_0}$$

where $\dot{\sigma}$ is the true stress and $\dot{\epsilon}$ is the true strain.

The true stress-true strain relation is commonly used as the material response curve in conjunction with a particular constitutive formulation. The constitutive formulation translates this one-

dimensional representation of the material response into arbitrary three-dimensional states of deformation. Ductile metals, which as a class of materials includes many weld metals, deform to such a degree that the uniaxial nature of the deformation is lost when the specimen begins to neck. The necking phenomenon invalidates the interpretation of $\bar{\sigma} - \bar{\epsilon}$ as the material's unaxial response. The actual uniaxial material true stress-true strain curve, valid at the continuum scale, can be obtained through procedures outlined in Matic (1985) and Matic, Kirby and Jolles (1986). The procedures treat the continuum true stress-true strain curve, denoted as the $\sigma - \epsilon$ curve, as the unknown parameter in an iterative series of computational simulations of the tensile specimen response. After each simulation, the predicted specimen response is compared to the laboratory specimen response. When satisfactory agreement is reached between predicted and observed specimen response, the solution curve is adopted for the material response.

An understanding of tensile specimen neck development was gained from these studies. They suggest that neck development is a consequence of the natural interaction between specimen geometry, applied load and the material true stress-true strain curve nonlinearity. With this view, necking develops without the need of auxiliary conditions to supplement the basic problem statement of geometry, load and material behavior. Traditionally, auxiliary conditions have been used to overcome incomplete material chraacterization in the form of inaccurate extrapolations of low strain $\bar{\sigma} - \bar{\epsilon}$ data into higher strain ranges beyond those encountered at the onset of necking. One of these auxiliary conditions has been the introduction of a geometric taper into the specimen geometry. This served to predispose the neck into developing at the narrowest point of the specimen gage length.

Without the need for artificial geometric imperfections to account for necking, the role of physically relevant geometric imperfections on tensile specimen response could be studied. In this investigation, computational simulations of HY-100 weld metal tensile specimen responses were examined. Defect radius and defect location on the specimen axis were selected as independent variables for a parametric study of their effect on the specimen response. The defect radii selected for the study were one order of magnitude smaller than the specimen diameter, in the range of currently available non-destructive inspection capability. Primary interest was on the role of the defect size and location on

3

specimen deformation asymmetry and the apparent ductility exhibited by the specimen. The concern regarding specimen asymmetry was motivated by the design of specimens with which to obtain effective material responses. The apparent ductility of the specimen relates directly to defect criticality and the translation of fabrication quality to structural integrity prediction.

A standard cylindrical tensile specimen geometry was selected for the computational simulations (Fig. 1). The gage section measured 5.08 cm (2.00 in.) in length and 1.27 cm (0.50 in.) in diameter. Including the grip sections, the entire specimen measured 12.70 cm (5.00 in.) in length and 1.65 cm (0.65 in.) in diameter at the grips. A typical void for purposes of analysis is shown.

CONTINUUM MATERIAL TOUGHNESS CONCEPTS

Tensile specimen failure will be initiated by the first occurrence of continuum fracture in the specimen. To accurately and consistently account for continuum fracture, the material fracture toughness must be defined accordingly. From fundamental considerations of thermodynamic consistency, *physical relevancy and geometric scale independence, energy is an appropriate quantity which satisfies* these requirements. The discussion in this section focuses on the statement of a strain energy density continuum fracture criterion and outline its application to tensile specimen failure prediction. For the purpose of this study, fracture initiation will be considered as specimen failure in view of the fact that the time between initiation and failure is generally short compared to the prior deformation history.

A continuum volume of material undergoing deformation is characterized by its multiaxial stress state σ_{ij} and multiaxial strain state ϵ_{ij}. For ductile metals, which exhibit inelastic deformation, the strain state is a function of the stress state and stress history. Then, the state of stress and strain may be related by a constitutive formulation which defines strain increments $d\epsilon_{ij}$ from the current stress state.
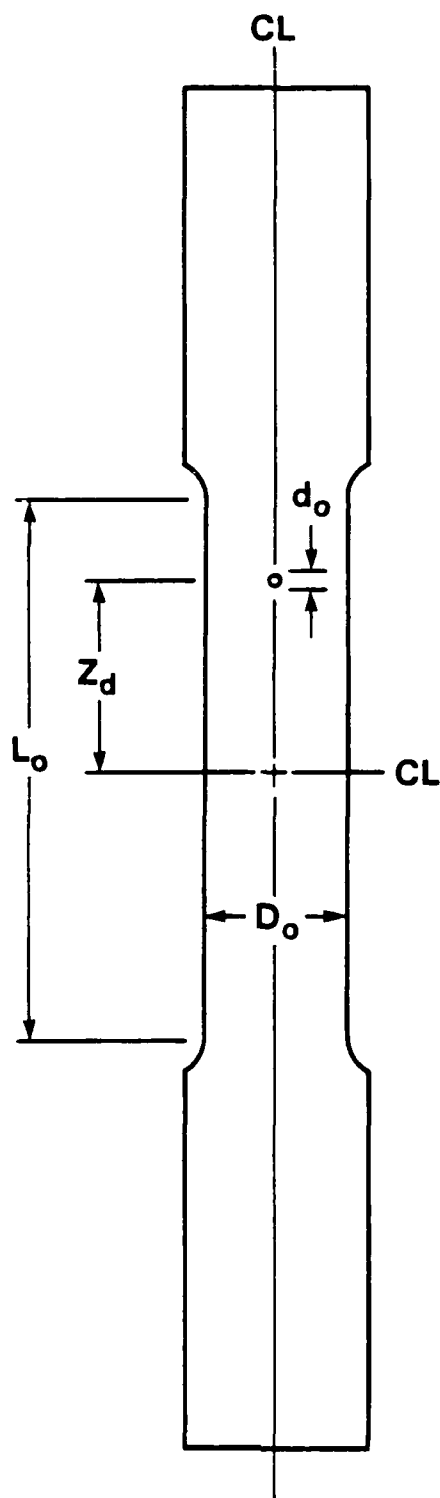
STANDARD TENSILE TEST SPECIMEN -

5.08 cm (2.00 in.) GAGE LENGTH L_o

1.27 cm (0.50 in.) DIAMETER D_o

PARAMETERS -

DEFECT LOCATION Z_d

$$0 \leqslant Z_d \leqslant \frac{L_o}{2}$$

DEFECT SIZE d_o

0.64 mm (0.025 in.)
0.89 mm (0.035 in.)
1.02 mm (0.040 in.)
1.27 mm (0.050 in.)
1.65 mm (0.065 in.)

Fig. 1 — Cylindrical tensile test specimen containing spherical void defect

The strain energy per unit mass at a given instant during deformation, will be

$$w = \lim_{\Delta V \to 0} \left[\frac{1}{\rho} \frac{\Delta W}{\Delta V} \right] \qquad (1)$$

$$= \int_0^{\epsilon_{ij}} \frac{\sigma_{ij}}{\rho} d\epsilon_{ij} \qquad (2)$$

where ρ is the mass density. This energy density incorporates both stress and strain into a fundamental quantity relevant to thermodynamic descriptions of material deformation and damage. The energy density is a scalar quantity which takes into account all components of the stress and strain tensors in a physically consistent manner. Failure of the material, at the continuum scale, can be associated with the value of the energy density at which fracture occurs. Thus, the material toughness is defined as

$$\omega_c = \int_0^{(\epsilon_{ij})_c} \frac{\sigma_{ij}}{\rho} d\epsilon_{ij} \qquad (3)$$

where w_c is the critical strain energy density value. The value of w_c, for engineering purposes, can be taken as material constant. This makes w_c independent of the particular deformation state and is a unifying feature absent in failure criteria based on stress alone or strain alone.

For ductile metals, the material density varies only slightly, even over large deformations. For this reason, it is common to define an energy per unit volume density

$$w = \lim_{\Delta V \to 0} \left[\frac{\Delta W}{\Delta V} \right] \qquad (4)$$

$$= \int_0^{(\epsilon_{ij})} \sigma_{ij} d\epsilon_{ij} \qquad (5)$$

with an associated critical value

$$w_c = \int_0^{(\epsilon_{ij})_c} \sigma_{ij} d\epsilon_{ij} \qquad (6)$$

The energy per unit mass is fundamental, but the energy per unit volume is equally appropriate for constant volume deformation processes.

For the case of a uniaxial true stress-true strain curve, corresponding to a one-dimensional state of deformation, the critical energy density corresponds to the area under the uniaxial stress-strain curve, i.e.

$$w_c = \int_0^{\epsilon_c} \sigma \, d\epsilon \qquad (7)$$

This representation is desirable for use with traditional constitutive formulations which rely on uniaxial stress-strain curves.

For a multiaxial state of stress, each of the six stress-strain pairs, three normal and three shear, must be evaluated and summed, i.e.

$$w_c = \int_0^{(\epsilon_{11})_c} \sigma_{11} \, d\epsilon_{11} + \int_0^{(\epsilon_{22})_c} \sigma_{22} \, d\epsilon_{22} + \int_0^{(\epsilon_{33})_c} \sigma_{33} \, d\epsilon_{33}$$

$$+ \int_0^{(\epsilon_{12})_c} \sigma_{12} \, d\epsilon_{12} + \int_0^{(\epsilon_{23})_c} \sigma_{23} \, d\epsilon_{23} + \int_0^{(\epsilon_{31})_c} \sigma_{31} \, d\epsilon_{31}$$

It should be noted that one or more individual terms in the multiaxial expression can be negative. Their total, w_c, must be positive, however.

A complete tensile specimen failure prediction should include the location of fracture initiation and the value of the applied load at which failure occurs. No a priori selection of the fracture initiation site should be made. Any material point in the specimen, either adjacent to or remote from the void defect, is a candidate failure site. The continuum toughness of the HY-100 weld metal can be determined from a defect free tensile test, and the results expressed in terms of the critical energy density value w_c.

A maximum value of the energy density will, in general, exist in the specimen. A relative energy density ratio may be defined by dividing the energy density w, attained during the loading process, by

the critical energy density, w_c. When values of this ratio are less than unity fracture initiation does not occur, i.e.

$$\left[\frac{w}{w_c}\right] < 1$$

at each point in the specimen.

As the load is increased, the specimen will continue to deform. When the relative energy density ratio reaches unity at a point so that

$$\left[\frac{w}{w_c}\right] = 1 ,$$

continuum fracture occurs. By normalizing the energy density throughout the structure with the critical energy density the relative tendency for fracture to occur at different points in the structure can be quantified.

COMPUTATIONAL SIMULATION

One half of the tensile specimen was modeled to take advantage of the axisymmetry of the problem. The ABAQUS finite element code was used (Hibbitt et al., 1984b). The model was composed of 732 elements, all type CAX8H (Fig. 2). These are axisymmetric 8-noded quadrilateral elements. Two degrees of freedom per node reflect radial and axial displacements. A single degree of freedom at each of nine element integration points is associated with an independently interpolated hydrostatic stress. The use of these hybrid elements prevented physically unrealistic displacement constraints from propagating through the grid. Such constraints can lead to artificially "stiff" responses of standard elements for incompressible or nearly incompressible deformations.

The HY-100 weld metal uniaxial continuum true stress-true strain curve is given in Fig. 3. This curve was developed from standard tensile data using the procedures outlined above. The critical energy density was calculated to be 4.11×10^8 N-m/m^3 (59,600 lb-in./in^3). This value was used to determine the fracture initiation site and instant of specimen failure.

d_o

(b)

(a)
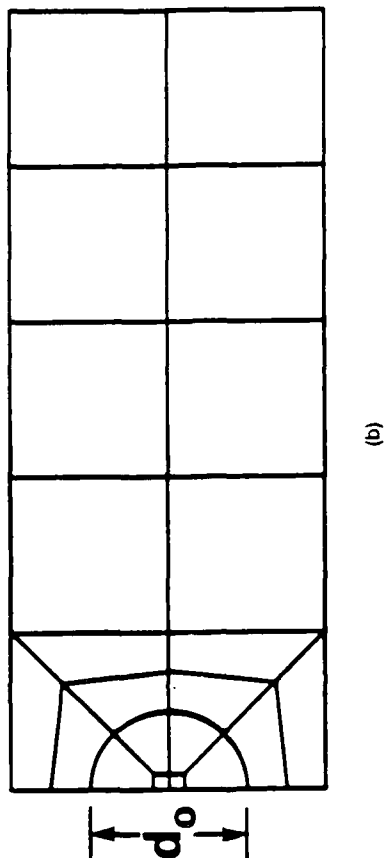
Fig. 2 — Axisymmetric finite element model. (a) Tensile specimen with 21 candidate defect sites. (b) Detail of typical defect site.

TRUE STRESS $\sigma \times 10^9$ N/m²

TRUE STRESS $\sigma \times 10^3$ lb/in²

TRUE STRAIN ε
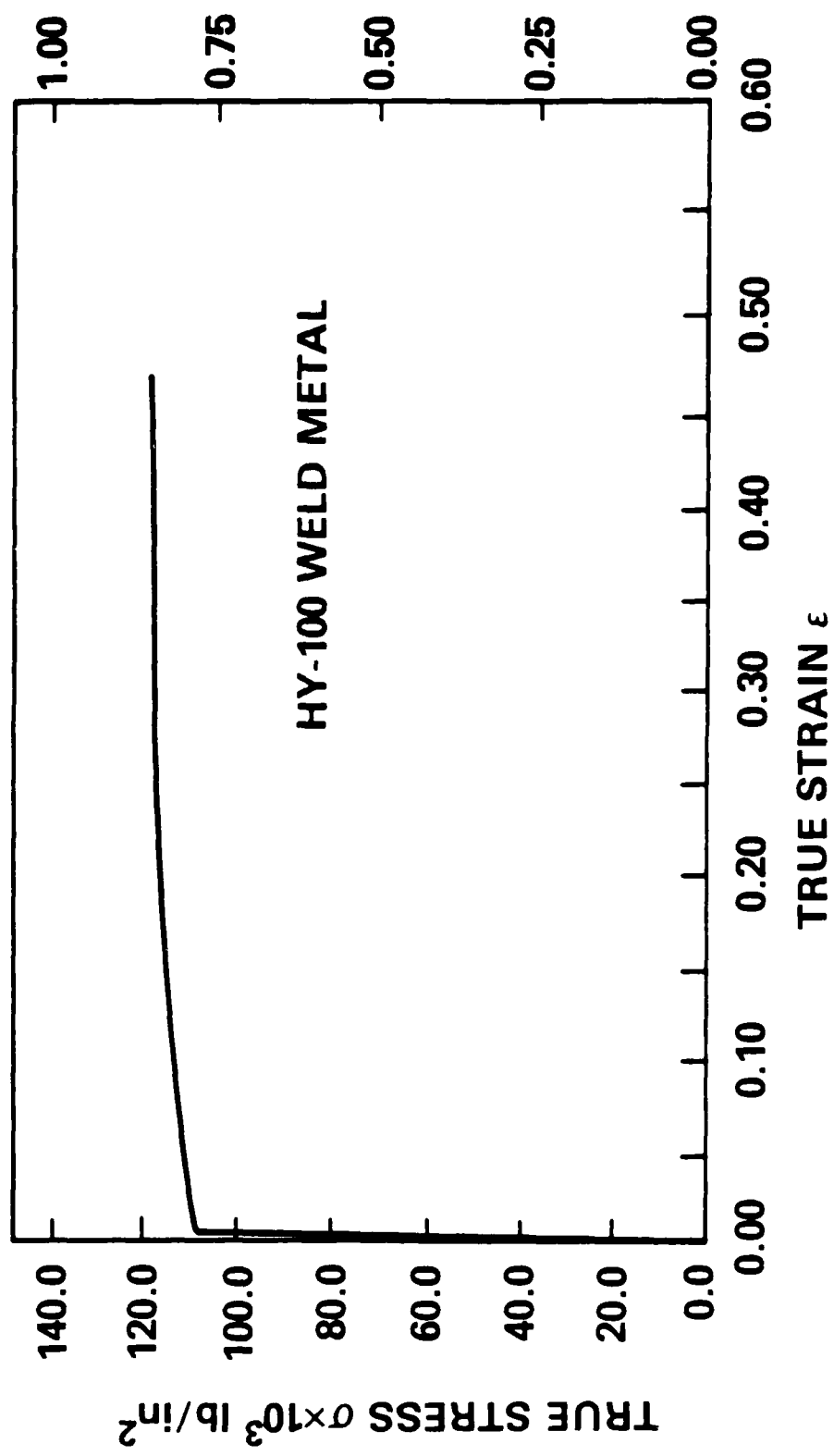
HY-100 WELD METAL

Fig. 3 — Uniaxial continuum true stress-true strain curve for HY-100 weld metal

Candidate sites for spherical void defect locations were introduced at 21 locations along the axis of the model. In a given analysis, 20 of the 21 candidate defect sites were retained as weld material. One of the 21 sites was transformed into a void by an ABAQUS option which reduces the element stiffness to zero over a small load increment. This option was invoked at the onset of deformation, effectively creating one void per specimen. Voids with diameters of 0.64, 0.89, 1.02, 1.27 and 1.65 mm (0.025, 0.035, 0.040, 0.050 and 0.065 in.) were generated in this manner (Fig. 4). The void diameters are approximately one-tenth of the specimen diameter, comparable to non-destructive inspection capability.

The candidate defect location along the axis were 2.54 mm (0.10 in) apart. Over the entire parametric series of analyses, voids were created at seven different locations, 2.54 mm to 17.8 mm (0.10 in. to 0.70 in.) from the horizontal centerline. No defects were necessary below the centerline since all were reflections of those above the centerline. The finite element mesh included all twenty-one defect sites to preserve discretization symmetry, thus ruling out discretization asymmetry as a factor in the results presented below.

Boundary conditions for the model were developed to closely duplicate the actual manner in which a tensile specimen is physically loaded. For the portion of the model corresponding to the lower grip, nodes along the outside surface were constrained to zero vertical displacement. For the portion of the model corresponding to the upper grip, nodes along the outside surface were given uniform vertical displacement. Thus, the lower grip constrained the specimen and the upper grip drove the specimen deformation.

For completeness, it should be mentioned that nodes interior to a generated void boundary were constrained to "drift" with the periphery of the void in an averaged sense. This prevented gross deformations of the zero stiffness elements caused by the combination of zero displacement of the nodes interior to the void and the continued deformation of the stiff model outside the void, and associated integration point Jacobian difficulties in the zero stiffness elements.
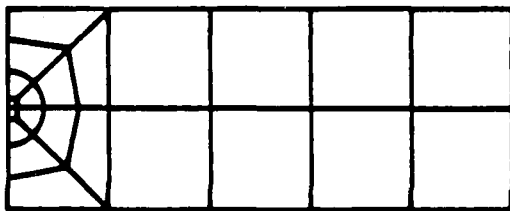
All analyses were performed with full geometric nonlinearity to account for large strains and rotations. An updated Lagrangian formulation is used for incremental solutions in ABAQUS . Rik's algo-
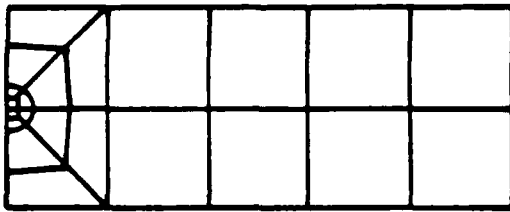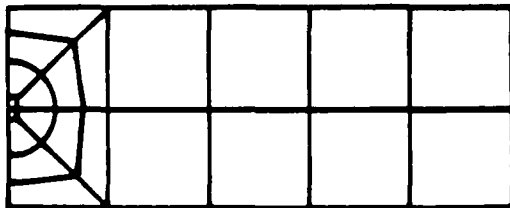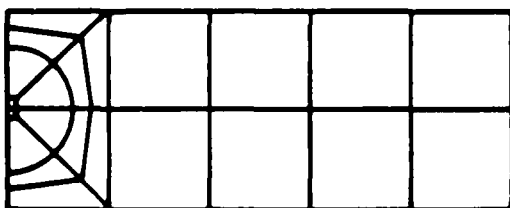
$d_o = 0.64$ mm (0.025 in.)
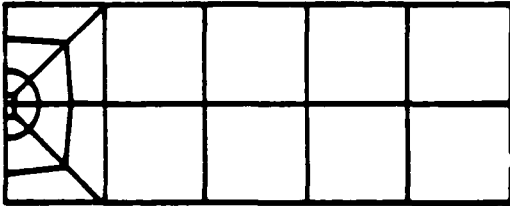
$d_o = 0.89$ mm (0.035 in.)

$d_o = 1.02$ mm (0.040 in.)

$d_o = 1.27$ mm (0.050 in.)

$d_o = 1.65$ mm (0.065 in.)

Fig. 4 — Finite element model details for spherical void defects of different diameter d_o

rithm, which is load displacement controlled, was used to ensure numerical stability, since the load P can be expected to decrease for large specimen elongations.

An incremental, rate independent plasticity theory was used for the material constitutive model (Hibbitt et al., 1984a). Total strains in the multiaxial strain state ϵ_{ij} a d uniaxial strain state ϵ are linearly decomposed into elastic and plastic components, i.e.,

$$\epsilon_{ij} = \epsilon_{ij}^e + \epsilon_{ij}^p$$

and

$$\epsilon = \epsilon^e + \epsilon^p.$$

The yield function f takes the form

$$f(\sigma_{ij}) = \sigma(\epsilon^p)$$

where σ_{ij} and σ are multiaxial stress states, respectively. The associated flow rule governs plastic strain increments by the relation

$$d\epsilon_{ij}^p = \lambda \frac{\partial f}{\partial \sigma_{ij}} .$$

In the case of purely elastic behavior $\lambda = 0$. For active yielding,

$$\lambda = d\epsilon^p \left| \frac{\sigma}{\sigma_{ij} \dfrac{\partial f}{\partial \sigma_{ij}}} \right| > 0$$

Plastic strain increments also satisfy a dissipation equivalence condition

$$\sigma d\epsilon^p = \sigma_{ij} d\epsilon_{ij}^p$$

and a consistency condition

$$\frac{\partial f}{\partial \sigma_{ij}} d\sigma_{ij} - \frac{\partial \sigma}{\partial \epsilon^p} d\epsilon^p = 0.$$

The von Mises yield function

$$f(\sigma_{ij}) = \frac{3}{2} \left(s_{ij} s_{ij} \right)^{1/2}$$

13

was employed. The deviatoric stress s_{ij} is defined as

$$s_{ij} = \sigma_{ij} - \frac{1}{3}\sigma_{kk}\sigma_{ij}.$$

where they hydrostatic component of stress is a $\sigma_{kk}/3$.

DISCUSSION OF RESULTS

As the first series of computational simulations were performed, for the 1.27 cm (0.50 in.) void defect diameter, noticeable trends in the specimen deformation became apparent. These trends were confirmed by the other simulations for 0.64, 0.89, 1.02, 1.27 and 1.65 mm (0.025, 0.035, 0.040, 0.050 and 0.065 in.) diameter void defects.

The deformed specimen shapes are plotted in Fig. 5. The defect location Z_d in the specimen was used to locate the figures in the horizontal direction. The defect size was used to locate the figures in the vertical direction. The asymmetry of the deformation is evident in many of the specimens, as is the variation in specimen ductility. These features will be quantified in discussions below. The neck location and the boundary between comparatively high and low ductility specimens are identified on this figure to illustrate both of these trends in a comprehensive manner.

Specimen deformation asymmetry, viewed in terms of the neck location, was directly related to the presence of a void defect. From the previous investigations discussed above on ideal, homogeneous specimens with the length-to-diameter ratio of four as considered here, deformation symmetry exists in the absence of any defects. The presence of the defect, however, tends to reduce the radial constraint of the specimen at the defect. This loss of constraint is in addition to the natural lack of constraint at the center of the gage length which can be attributed to the geometry of the specimen. For defect locations near the center of the specimen, these two sources of low constraint coincide in a constructive manner to draw the neck deformation toward the defect. For defect locations farther from the center of the specimen, the presence of the grip section adjacent to the gage section tends to negate the influence of the defect. The radial constraint generated by the grip sections tends to offset the lack

LOW
DUCTILITY
HIGH
DUCTILITY

1.65 mm (0.065 in.) DIA.
VOID DEFECT

1.27 mm (0.050 in.) DIA.
VOID DEFECT

1.20 mm (0.040 in.) DIA.
VOID DEFECT

0.89 mm (0.035 in.) DIA.
VOID DEFECT

0.64 mm (0.025 in.) DIA.
VOID DEFECT

CENTER	0.1	0.2	0.3	0.4	0.5	0.6	0.7	inches
OF GAGE								
LENGTH								centimeters

0.5   1.0   1.5   2.0
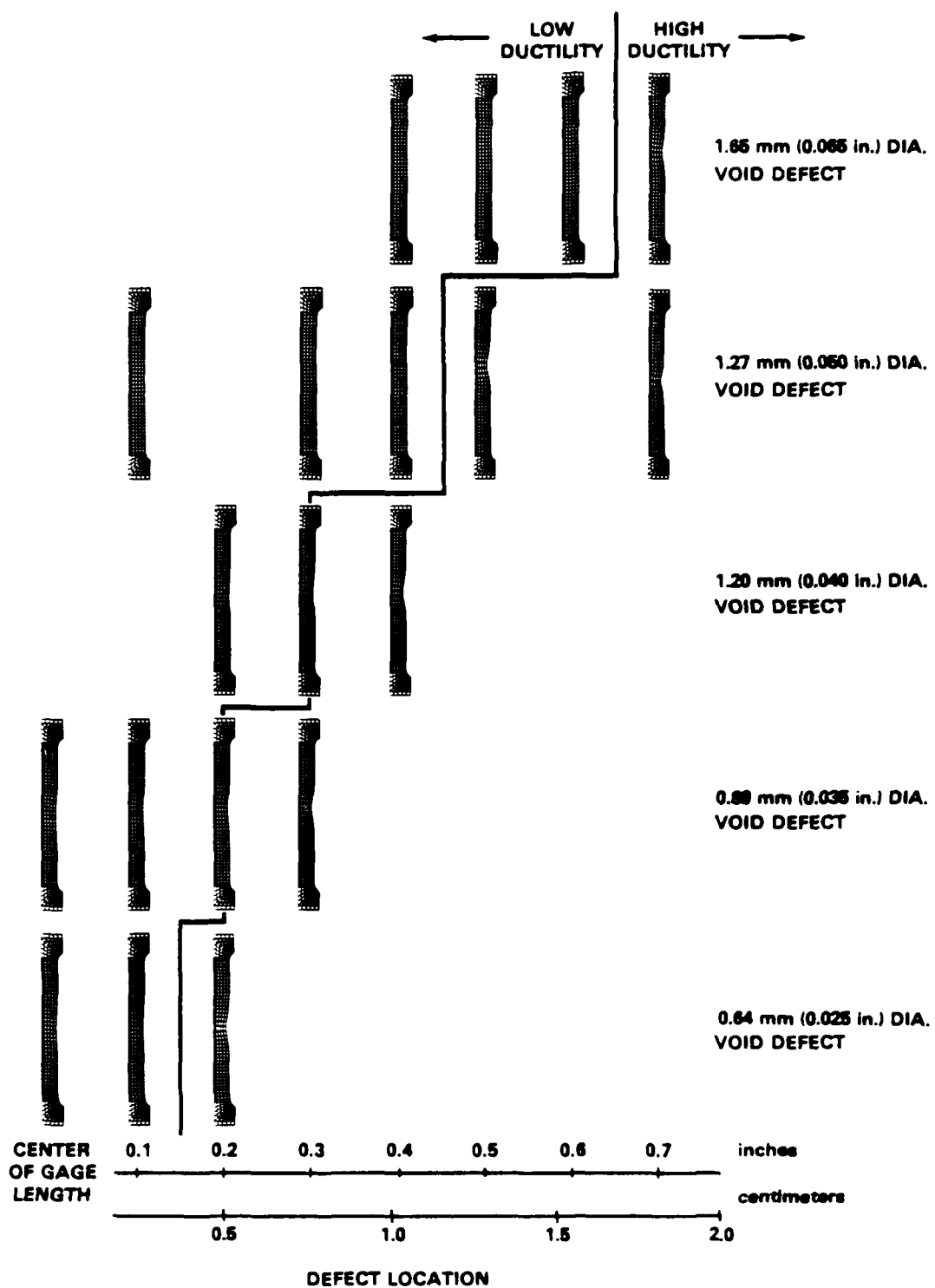
DEFECT LOCATION

Fig. 5 — Predicted specimen deformation for different spherical void defect locations and diameters

of constraint produced by the defect. As a result, for these cases, the neck location tends to move back toward the center of the specimen as the defect is located closer toward the grip section.

The neck location Z_n is plotted against the defect location Z_d in Fig. 6, with defect size as a parameter. Both Z_n and Z_d are expressed with reference to the undeformed tensile specimen geometry. If the defect dominates the neck development completely, this neck localization plot should lie on a line of slope one and intersect the origin. If the neck is insensitive to the defect, symmetric specimen deformation results and the line falls on the Z_d axis.

It is apparent from the simulations that the defects near the center of the specimen, at small Z_d values, tend to strongly influence the neck location. Defect size, however, plays a dominant role over the rate at which this effect diminishes. For the 1.65 mm (0.065 in.) diameter defect, its location dictates the neck location over fully one half of the specimen length. For the 0.64 mm (0.025 in.) diameter defect, the effect is essentially insignificant as the neck remains at the center of the specimen.

For all the specimens, whether a relatively large or small defect is present, the neck localization curve drops toward the Z_d axis as Z_d increases. This coincides with the radial constraint adjacent to the grips and overwhelms the tendency of the defect to reduce constraint. The maximum value of each curve increases with the defect size. The maximum moves towards the origin as the defect size grows smaller. The maximum moves towards the diagonal line as the defect size grows larger. The locus of these maximum points form a curve which should be asymptotic to the Z_d axis for small Z_d values and asymptotic to the diagonal line for large Z_d values.

The apparent ductility of the specimen was measured by the percent reduction of area (% RA) at failure. From the asymmetric behavior of the specimens, it is apparent that whether the neck volume of the specimen contains the void defect depends on the size and location of the defect. For the case when the defect and neck volume do not coincide, the deformation and resulting energy density levels at the interior of the neck first rise to the critical energy density. The local neck deformation develops essentially as it would in the absence of the defect. As a result, the specimen ductility matches that of a defect free specimen. For the cases when the two coincide, the combined effect of the void stress,
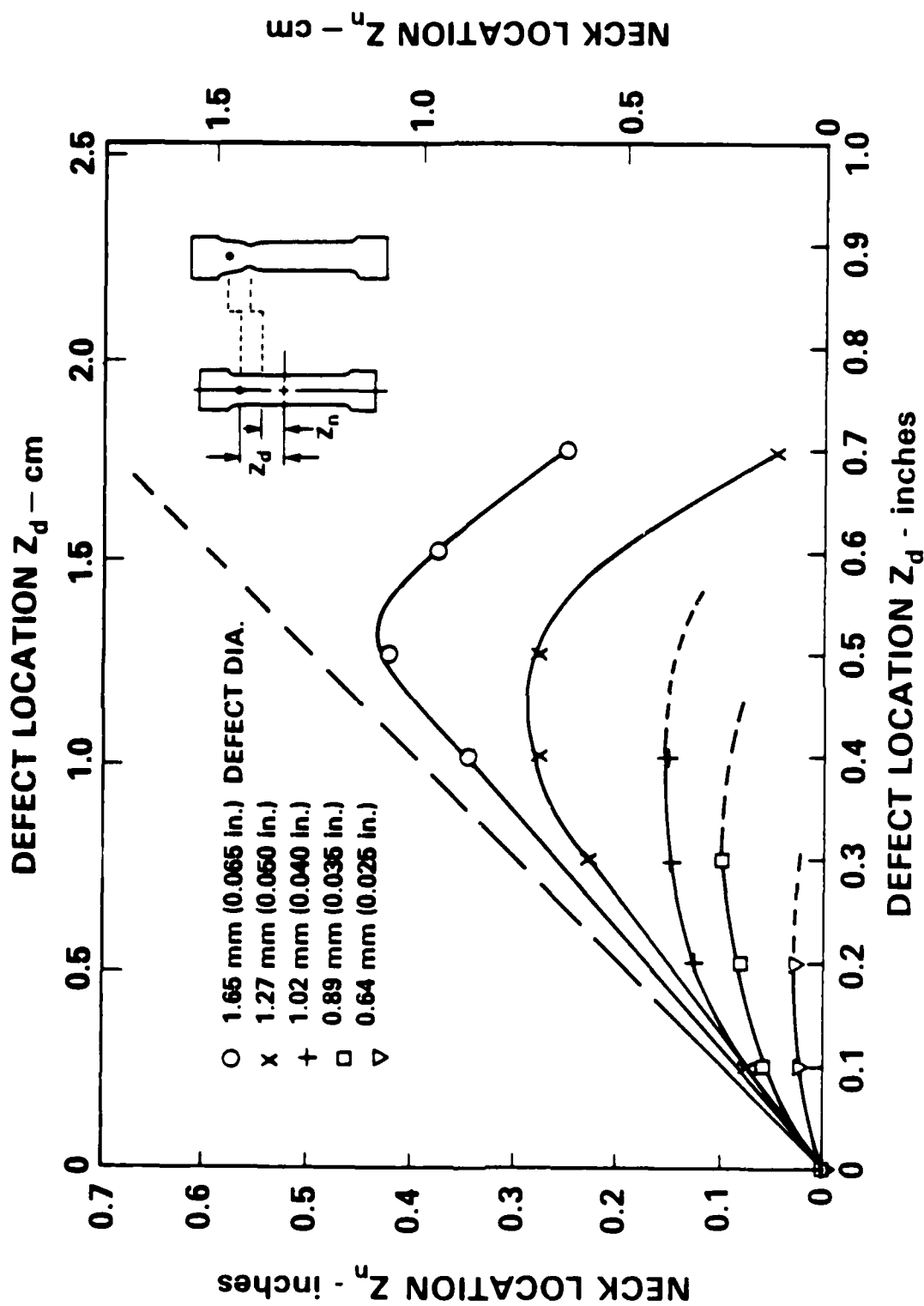
Fig. 6 — Predicted specimen neck location versus spherical void defect location

strain and energy concentration and the lateral contraction of the neck volume produces fracture initiation at the periphery of the void much quicker than for neck deformation alone. Initiation occurs when the energy density reaches the critical value at this location. As a result, the specimen ductility is significantly reduced for the range of defect sizes and locations which coincide with the neck development. The percent reduction of area

$$\% \ RA = \frac{A_0 - A_f}{A_0} \times 100$$

is plotted against the defect location Z_d for each specimen (Fig. 7). For those combinations of defect size and location where the neck deformation and defect location do not coincide, the full specimen ductility of approximately 35% RA is attained. Full specimen ductility is essentially independent of defect size since the specimen failure does not involve the defect.

For those combinations of the defect size and location where the neck deformation and defect location do coincide, the specimen ductility is markedly reduced. Since the specimen failure involves the defect, the energy concentration in the vicinity of the defect depends on the size of the defect. This is apparent in the precise values predicted for the % RA. For the largest defect considered, with a diameter of 1.65 mm (0.065 in.), the ductility was reduced to approximately 7% RA. This was reflected in the brittle appearance of the deformed specimen shapes in Fig. 5. As the defect size decreases, the ductility increases. For the smallest defect sizes considered, with diameters of 0.64 mm and 0.89 mm (0.025 in. and 0.035 in.), the RA rises to approximately 18%.

It is important to note that for each defect size considered, the ductility plot takes on one of only two values for each defect location. The high value is predicted for defects located near to the grip sections, and a low value for the defects located near to the center of the specimen. The transition between these two distinct values is sharp and abrupt. A considerable effort was undertaken to verify and characterize this transition. Without exception, the transition occurs over a defect location distance no greater than five percent of the specimen gage length. That is to say that a change in the defect location of only 2.54 mm (0.10 in.), for the standard tensile specimen geometry considered here, pro-
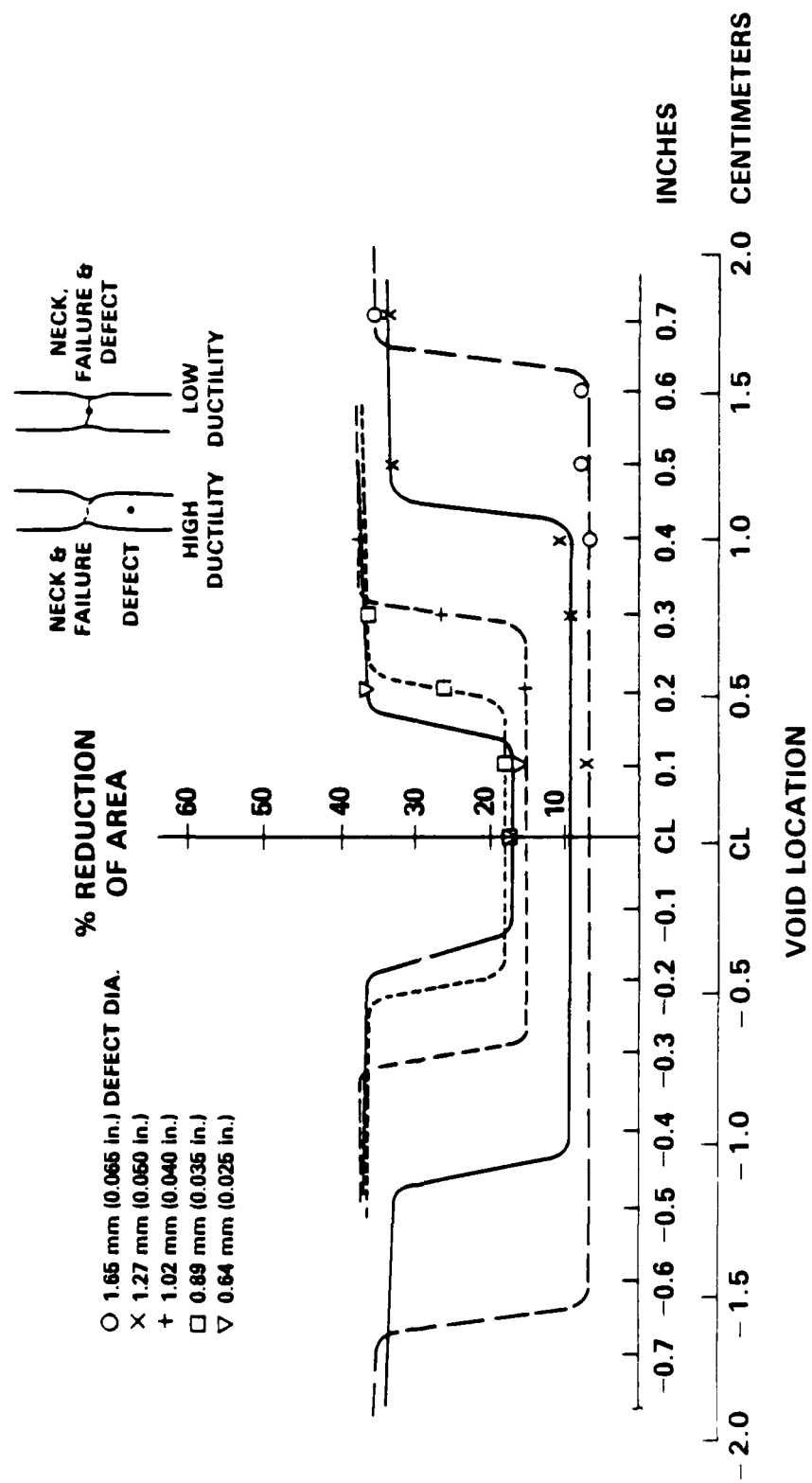
Fig. 7 — Specimen percent reduction of area versus spherical void defect location

duces the step increase or decrease in the specimen ductility. The sharpness of this transition is directly related to the location of the neck with respect to the defect.

The load-displacement plots for all specimens were essentially identical, except for the point at which failure occurred (Fig. 8). The point of failure for those specimens in which the neck and void defect are not coincident occurred for a specimen gage length deformation of approximately 5.08 mm (0.20 in.). This is the same as for a defect free specimen. The point of failure moves to smaller values of specimen gage length deformation as the defect diameter increases. For the largest defect considered, with diameter 1.65 mm (0.065 in.), the point of failure is at a deformation of approximately 1.27 mm (0.050 in.).

The results of the analyses can be used to assess the severity of each void defect size. The defects must be considered in the context of the specimen geometry, the actively deforming material in the neck and the ductility necessary for a minimum apparent toughness of the material. For example, a practical minimum required apparent toughness might coincide with 10 percent reduction of area. At this value, fracture initiates for relatively low stress, strain and energy values. Rapid crack growth could be expected to follow. The maximum apparent toughness, for a defect free neck volume, was associated with a 35 per cent reduction of area. Ductility within 10 percentage points of this value would be expected to still provide substantial resistance to fracture initiation and crack growth. The intermediate apparent toughness range, from 10 to 25 per cent reduction of area, may be classified as marginal toughness. The particular application and its tolerance to reduced apparent ductility should be considered so as to make quantitative predictions on the influence of defects to structural integrity prediction.

For the defects considered in this set of analyses, the two larger sizes, 1.65 mm and 1.27 mm (0.065 in. and 0.050 in.) in diameter, are critical (Fig. 9). The three smaller sizes, 0.63, 0.89 and 1.02 mm (0.025 in., 0.035 in. and 0.040 in.) in diameter, are marginal defects. The upper bound on defect diameter lies below 0.63 mm (0.025 in.).
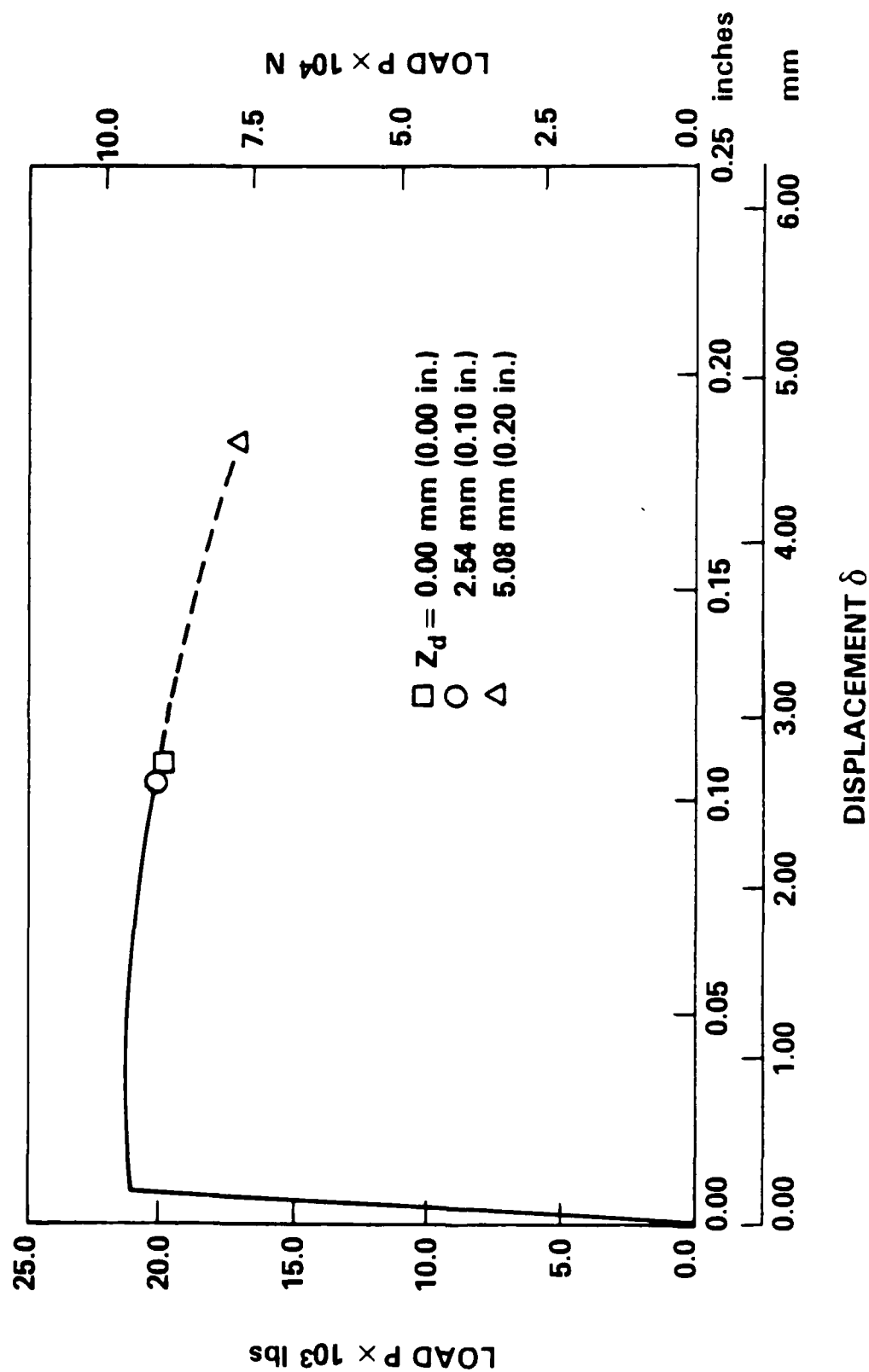
LOAD P × 10⁴ N

Fig. 8(a) Specimen load-displacement responses for different spherical void defect locations, Z_d. Spherical void defect diameter, d_v, of 0.64 mm.
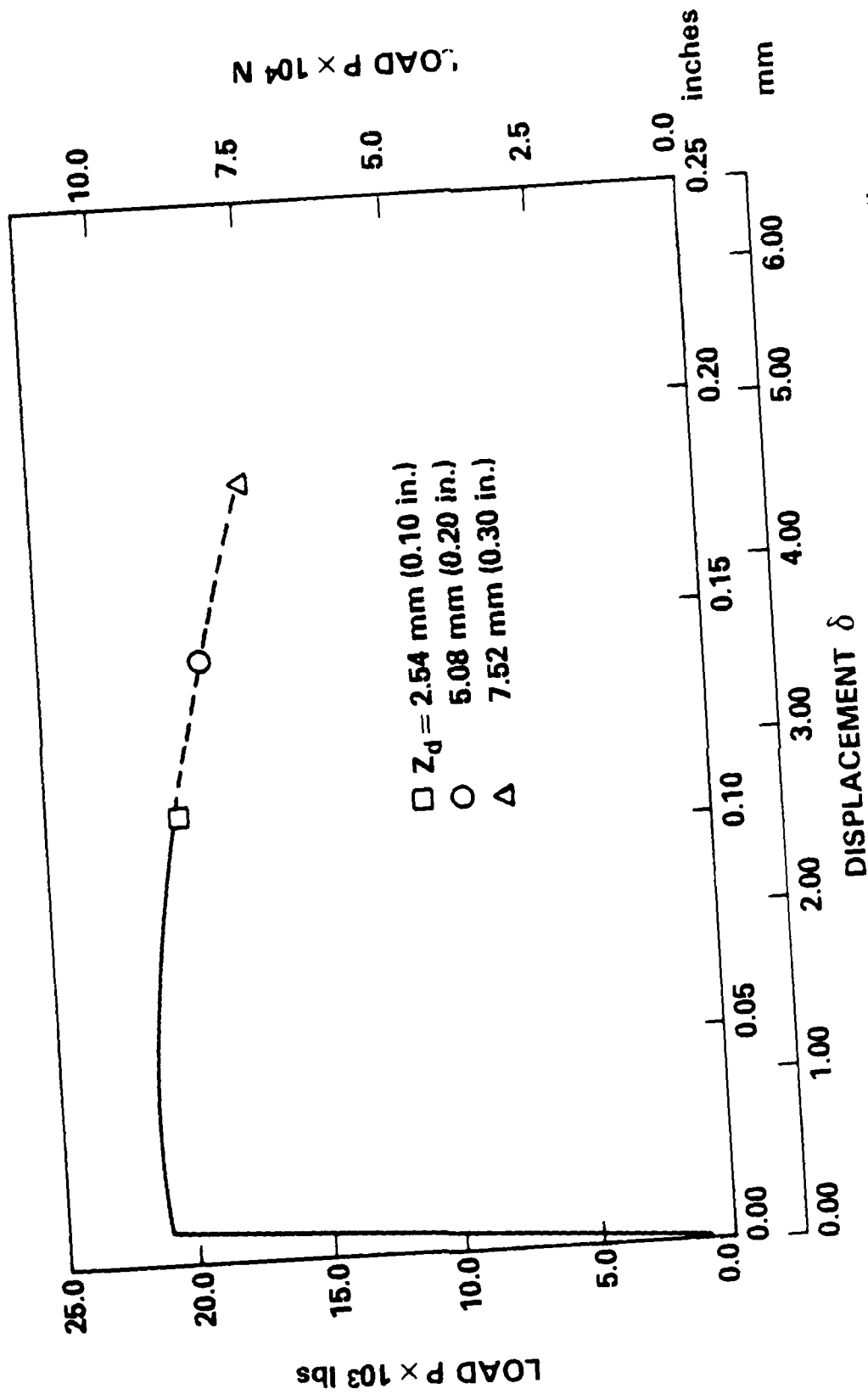
DISPLACEMENT δ

$\square$ Z_d = 0.00 mm (0.00 in.)
$\bigcirc$ 2.54 mm (0.10 in.)
$\triangle$ 5.08 mm (0.20 in.)

LOAD P × 10³ lbs

21

Fig. 8(b) Specimen load-displacement responses for different spherical void defect locations. Z_d. Spherical void defect diameter, d_v, of 0.89 mm.
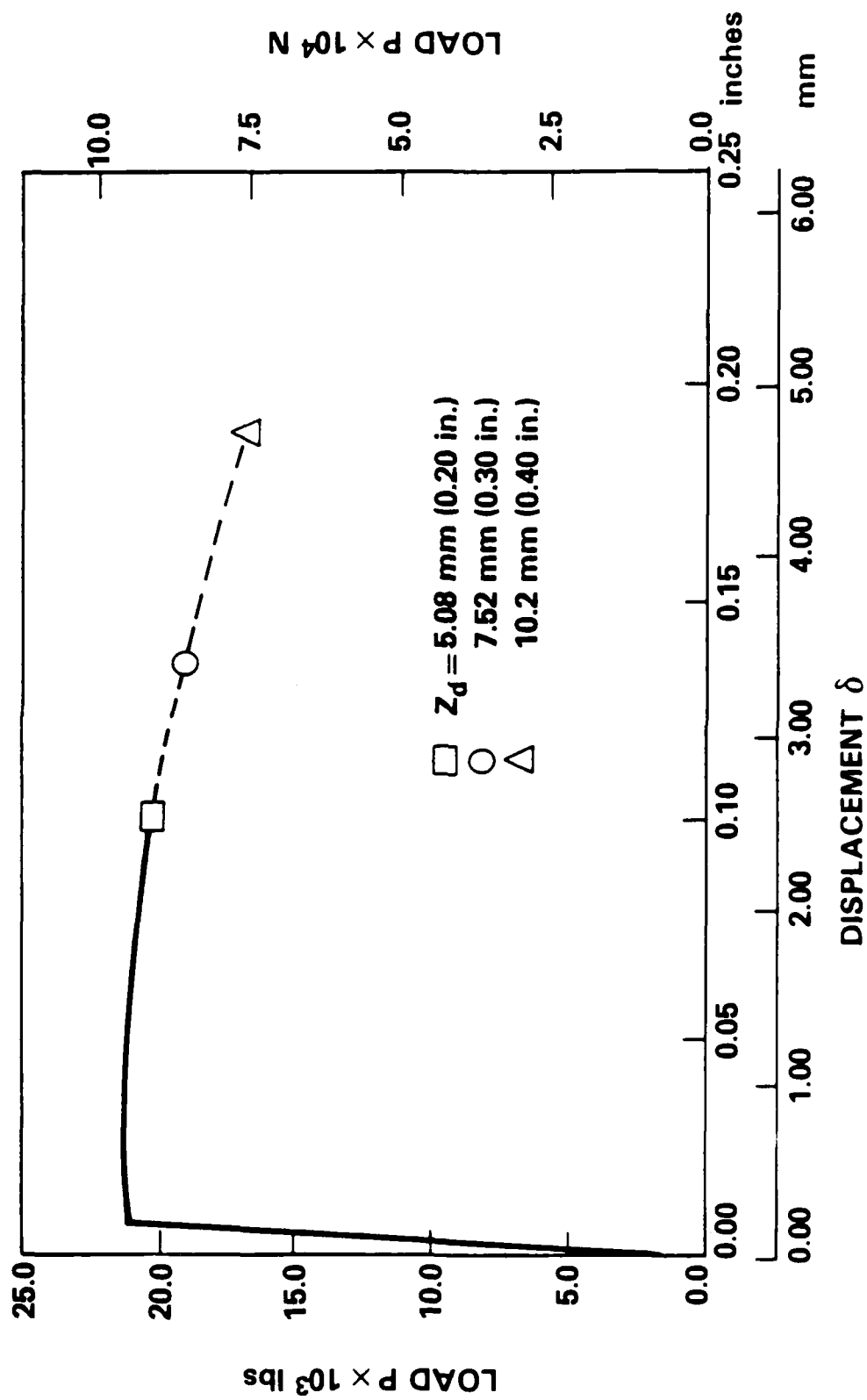
22

Fig. 8(c) Specimen load displacement responses for different spherical void defect locations, Z_d. Spherical void defect diameter, d_o, of 1.02 mm.
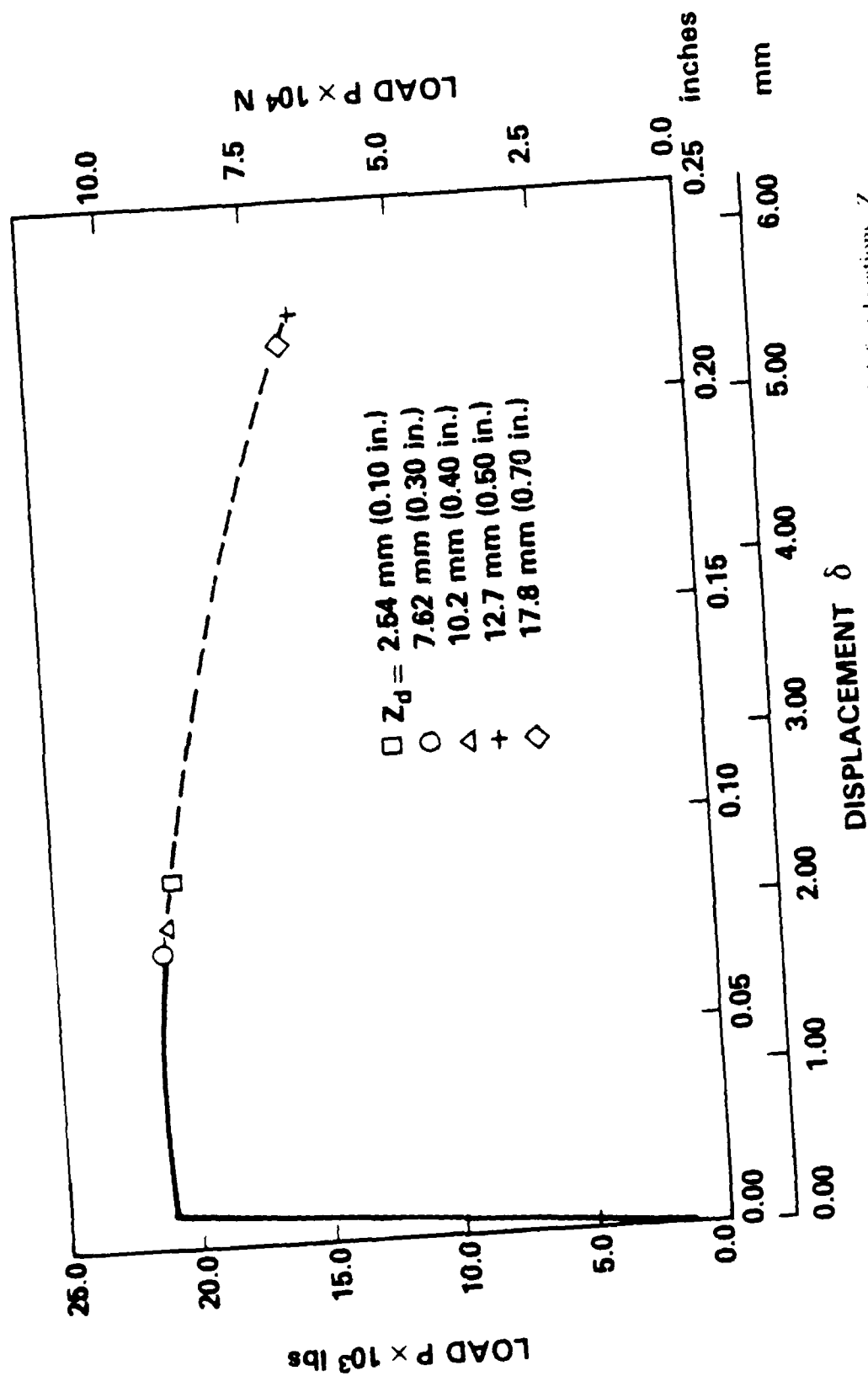
LOAD P × 10⁴ N

inches
mm

□ Z_d = 5.08 mm (0.20 in.)
○ 7.52 mm (0.30 in.)
△ 10.2 mm (0.40 in.)

DISPLACEMENT δ

LOAD P × 10³ lbs

Fig. 8(d)   Specimen load displacement responses for different spherical void defect locations, Z. Spherical void defect diameter, d_o, of 1.27 mm.
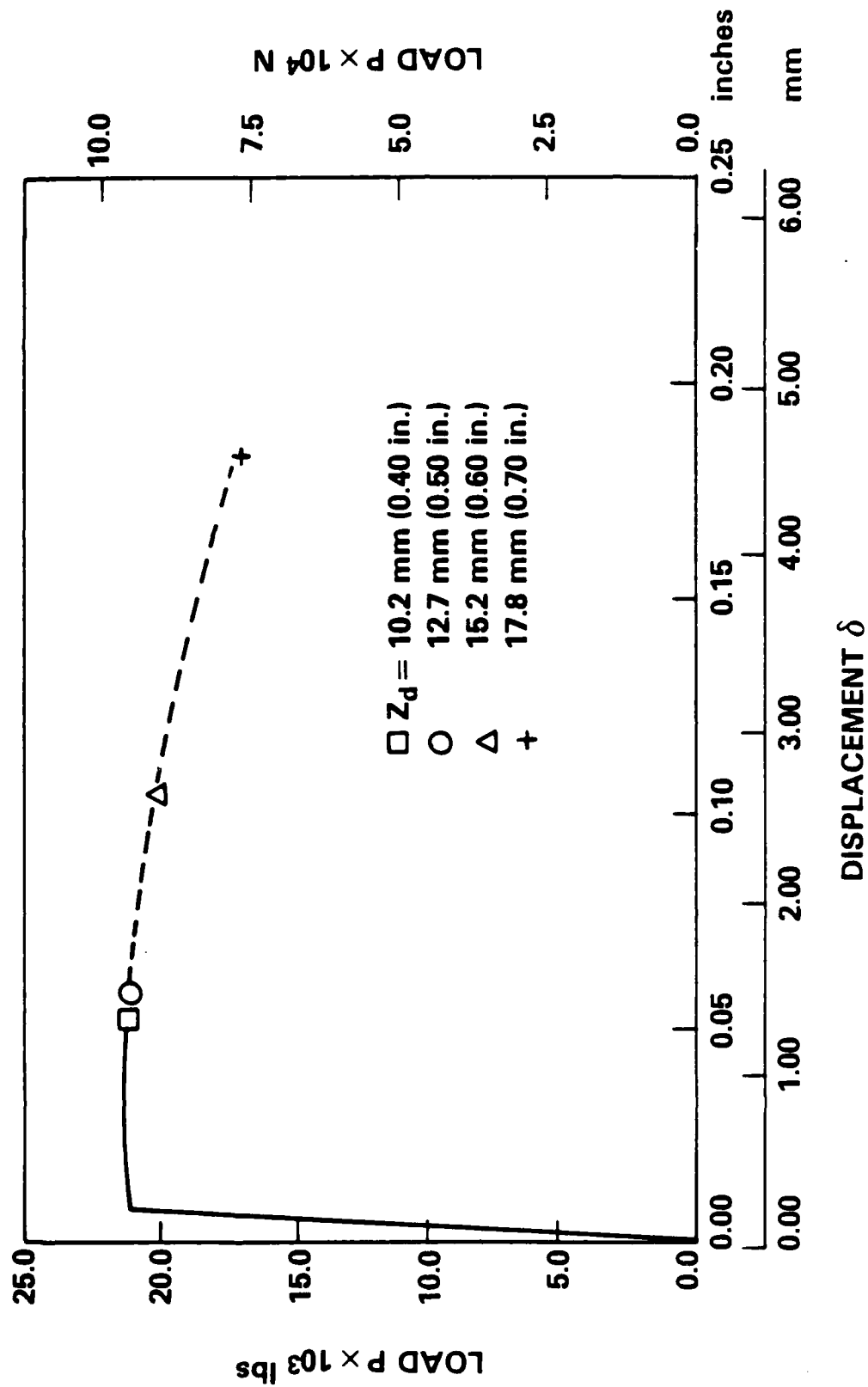
The figure shows a plot with axes:
- LOAD $P \times 10^4$ N (inches, mm)
- LOAD $P \times 10^3$ lbs
- DISPLACEMENT δ

Legend:
- □ $Z_d = 2.54$ mm (0.10 in.)
- ○ 7.62 mm (0.30 in.)
- △ 10.2 mm (0.40 in.)
- + 12.7 mm (0.50 in.)
- ◇ 17.8 mm (0.70 in.)

24

Fig. 8(e) — Specimen load-displacement responses for different spherical void defect locations, Z. Spherical void defect diameter, d_o, of 1.65 mm.

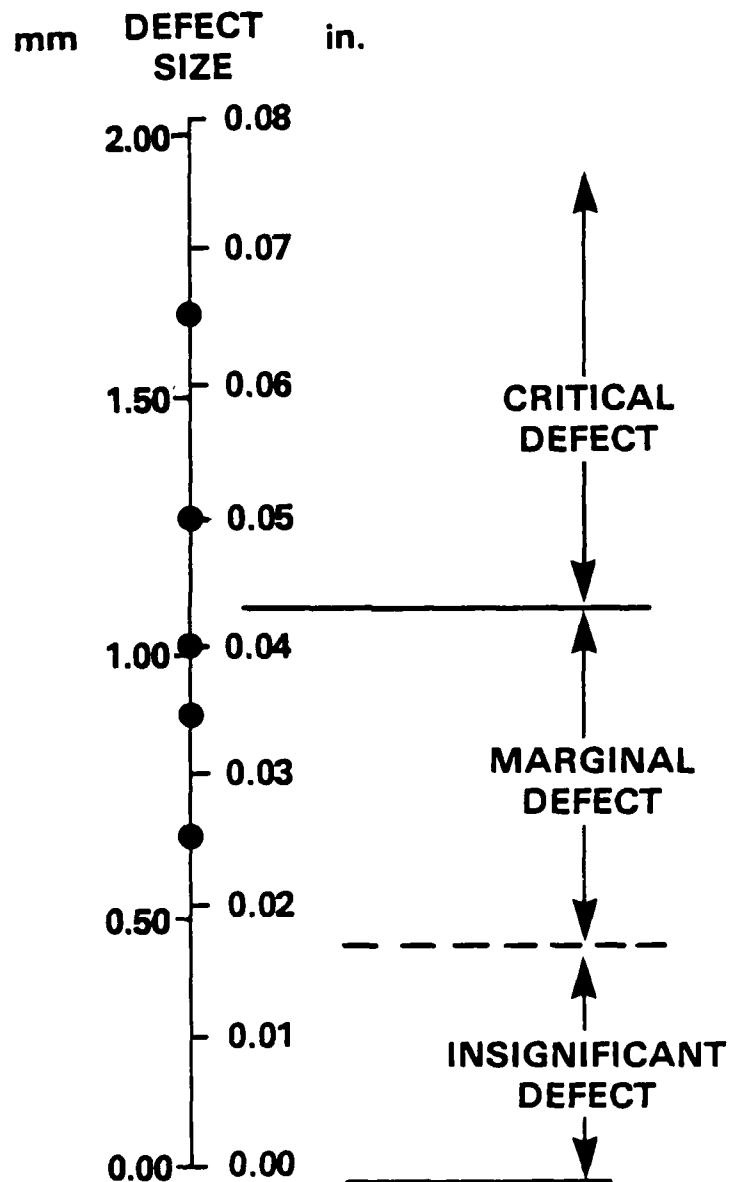# DEFECT SIZE CATEGORIZATION FOR HY-100 WELD METAL

Fig. 9 — Spherical void defect criticality assessment based on tensile specimen computational predictions

SUMMARY

The role of small spherical defect size and location on tensile specimen deformation asymmetry and ductility were quantitatively examined by computational simulation. The role of a defect in specimen asymmetry supports earlier findings in which specimen geometry, loading and material behavior are sufficient to cause necking, but the defect is shown to influence necking.

Specimen fracture occurs at the specimen neck in all cases. In the event the defect and neck volume coincide, the combined effect of the two stress concentrations is to cause a significant reduction in the specimen ductility. When defect and neck are not coincident, specimen ductility reverts back to the defect free full ductility.

The transition between full ductility and reduced ductility is sharp, and depends strongly on defect location within the specimen. For the defect diameters considered, this abrupt transition is sensitive to defect locations separated by a difference of five percent of the specimen gage length.

Quantitative defect classification is discussed in terms of apparent specimen ductilities and practical considerations to ensure structural integrity. Actual application of this type of information to a specific integrity problem depends, of course, on meaningful translation of the specimen behavior to effective material behavior in a structure. This aspect of the problem is currently under investigation.

REFERENCES

[1]   Boulton, C.F., 1977, "Acceptance Levels of Weld Defects for Fatigue Service," *Welding Journal,* Vol. 56 No. 1, pp. 13s - 22s.

[2]   Harrison, J.D., 1977a," Basis for a Proposed Acceptance—Standard for Weld Defects. Part 1: Porosity," *Met. Constr./ Br. Weld J.,* Vol. 4 No. 3, pp. 99-107.

[3]   Harrison, J.D., 1972b, "Basis for a Proposed Acceptance—Standard for Weld Defects. Part 2: Slag Inclusions," *Met. Constr./Br. Weld J.,* Vol. 4 No. 7, pp. 262-267.

[4]   Hibbitt, H.D., Karlsson, B.I. and Sorenson, E.P., 1984a, *ABAQUS Theory Manual*, Hibbitt, Karlsson and Sorenson, Inc., Providence, RI.

[5]   Hibbitt, H.D., Karlsson, B.I. and Sorenson, E.P., 1984b, *ABAQUS User's Manual*, Hibbitt, Karlsson and Sorenson, Inc., Providence, RI.

[6]   Lundin, C.D., 1983, "Discontinuities in Welds—Cause and Effect," *J. Materials for Energy Systems*, Vol. 5 No. 3, pp. 123-130.

[7]   Lundin, C.D., 1984, "Fundamentals of Weld Discontinuities and their Significance," *Welding Research Council Bulletin* 295.

[8]   Matic, P., 1985, "Numerically Predicting Ductile Material Behavior from Tensile Specimen Response," *Theoretical and Applied Fracture Mechanics*, Vol. 4, pp. 13-28.

[9]   Matic, P., Kirby, G.C. III and Jolles, M.I., 1986, "The Relationship fo Tensile Specimen Size and Geometry Effects to Unique Constitutive Parameters for Ductile Materials," *NRL Memo. Rpt.*

[10]   Wells, A.A., 1983, "The Meaning of Fitness-for-Purpose and the Concept of Defect Tolerance," *FWP J.*, Vol. 23 No. 12, pp. 43-56.

APPENDIX

ABAQUS Finite Element Program Formulation

A brief summary of the ABAQUS finite element program is included here for reference and completeness in view of the various possible theoretical formulations available for geometrically and materially nonlinear analysis. The reader is referred to Hibbitt et al (1984a) for further details.

For a material particle at reference position X_i at time t equal to zero, its current position x_i at a later time may be expressed as

$$x_i = x_i(X_i, t) . \qquad (A1)$$

An orthogonal coordinate system of unit base vectors is assumed. The relative position dx_i between two material particles in their current configuration may be expressed in terms of their relative position in their reference configuration

$$dx_i = \frac{\partial x_i}{\partial X_j} dX_j \qquad (A2)$$

$$= F_{ij} dX_j \qquad (A3)$$

where F_{ij} is defined as the deformation gradient.

The velocity of the material particle will be

$$v_i = \frac{\partial x_i}{\partial t} . \qquad (A4)$$

The incremental velocity between two particles will be

$$dv_i = \frac{\partial v_i}{\partial X_j} dX_j \qquad (A5)$$

$$= \frac{\partial v_i}{\partial x_j} \frac{\partial x_j}{\partial X_k} dX_k \qquad (A6)$$

$$= L_{ij} F_{jk} dX_k \qquad (A7)$$

29

where L_{ij} is the velocity gradient at a material point in the body. The velocity gradient may be decomposed into the sum of its symmetric and antisymmetric tensor components as

$$L_{ij} = \frac{1}{2}(L_{ij} + L_{ji}) + \frac{1}{2}(L_{ij} - L_{ji}) \tag{A8}$$

$$= \frac{1}{2}(v_{i,j} + v_{j,i}) + \frac{1}{2}(v_{i,j} - v_{j,i}) \tag{A9}$$

$$= D_{ij} + \Omega_{ij} \tag{A10}$$

where D_{ij} is the rate of deformation tensor, associated with material straining, and Ω_{ij} is the material spin tensor associated with pure rotation at the material point.

For a material body of volume V and surface S in its current configuration, force equilibrium in integral form is given by

$$\int_S t_i \, dS + \int_V f_i \, dV = 0 \tag{A11}$$

where t_i is the surface traction vector per unit of current area and f_i is the body force vector per unit of current volume. The Cauchy stress tensor σ_{ij} is related to t_i by

$$t_i = \sigma_{ij} n_j \tag{A12}$$

where n_j is the outward unit vector normal to surface S. Using (A12) in (A11) along with Gauss' theorem to transform the surface integral to a volume integral,

$$\int_V (\sigma_{ij,j} + f_i) \, dV = 0. \tag{A13}$$

The integral must, in general, be zero. Therefore,

$$\sigma_{ij,j} + f_i = 0. \tag{A14}$$

Moment equilibrium in integral form requires

$$\int_S x_i t_j e_{ijk} \, dS + \int_V x_i f_j e_{ijk} \, dV = 0 \tag{A15}$$

where e_{ijk} is the permutation symbol. Using Gauss' theorem

$$\int_V (x_{i,l} \sigma_{jl} e_{ijk} + x_i \sigma_{jl,l} e_{ijk} + x_i \sigma_{jl} e_{ijk,l} + x_i f_j e_{ijk}) \, dV = 0 \tag{A16}$$

30

Evaluating each term in this expression and using (A14) provides that σ must be symmetric, i.e.

$$\sigma = \sigma^T \tag{A17}$$

The differential force equilibrium expression (A14) is used to generate a virtual work expression by taking the dot product with a virtual velocity δv and integrating over the volume. This takes the form, after application of Gauss' theorem,

$$\int \left[\sigma : \dot{\varepsilon} - \rho \, \ddot{u} \cdot \delta v + \cdots \right] \, dV = 0 \tag{A18}$$

The virtual velocity field must satisfy continuity and prescribed velocity requirements. Expressing the first integral in terms of tractions and rearranging

$$\int \sigma : \dot{\varepsilon} \, dV = \int t \cdot \delta v \, dS + \int \cdots \tag{}$$

From the definition of the velocity gradient, the fact that

$$\cdots \tag{}$$

$$\cdots \tag{}$$

where the virtual rate of deformation

ght of the Cauchy stress tensor

$$\int \cdots$$

The left hand side of this expression

$\cdots$

$$\int \cdots$$

where J is the determinant of the

reference and current configuration.

The Kirchoff (or Trefftz) stress is

$$\cdots \tag{}$$

Therefore,

$$\int_{V_o} \tau_{ij} D_{ij}^* dV_o = \int_S t_i v_i^* dS + \int_V f_i v_i^* dV \qquad (A25)$$

The Kirchoff stress, τ_{ij}, is equal to the Cauchy stress, σ_{ij}, when J is equal to unity. For the material behavior considered in this analysis J deviates from unity by only a small amount. Therefore, the constitutive formulation in terms of Cauchy stress, as described in the main body of this paper will be applicable when expressed in terms of Kirchoff stress.

Equation (A26) is the virtual velocity equilibrium equation and is the basis for interpolation and discretization for the finite element formulation. The virtual velocity at a point inside an element will be interpolated as

$$v_i^* = N_{ij} \bar{v}_j^* \qquad (A26)$$

where the summation is understood to involve only those nodal values $\bar{v}_j^*$ relevant to a particular element. The virtual rate of deformation becomes

$$D_{ij}^* = \frac{1}{2}(N_{ik}\bar{v}_k^*)_{,j} + (N_{jk}\bar{v}_k^*)_{,i} \qquad (A27)$$

$$= \frac{1}{2}(N_{ik,j} + N_{jk,i})\bar{v}_k^* \qquad (A28)$$

Therefore, (A25) becomes

$$\int_{V_o} \frac{1}{2}\tau_{ij}(N_{ik,j} + N_{jk,i})\bar{v}_k^* dV_o = \int_S t_i N_{ik}\bar{v}_k^* dS + \int_V f_i N_{ik}\bar{v}_k^* dV \qquad (A29)$$

or, since $\bar{v}_k^*$ appears in each integral,

$$\int_{V_o} \frac{1}{2}\tau_{ij}(N_{ik,j} + N_{jk,i}) dV_o = \int_S t_i N_{ik} dS + \int_V f_i N_{ik} dV . \qquad (A30)$$

The integrations are taken with respect to the discretized volumes and surfaces consistent with element and nodal definitions.

Equation (A30) forms the basis for the finite element solution. An incremental solution is generated by the Newton algorithm. The Jacobian of (A30) is required for the incremental solution, and

results in the introduction of a Kirchoff stress rate, $\dot{\tau}_{ij}$, into the incremental equilibrium equation. The stress rate takes the form

$$\dot{\tau}_{ij} = \overset{\triangledown}{\tau}_{ij} + \Omega_{ik}\tau_{kj} + \tau_{ik}\Omega_{jk} \tag{A31}$$

where $\dot{\tau}_{ij}$ is the total stress rate, $\overset{\triangledown}{\tau}_{ij}$ is the material (or Jaumann) stress rate associated with the material response through the constitutive formulation. The remaining terms involving Ω_{ij} are stress rate contributions due to rotation. In practice, all constitutive calculations are performed using $\overset{\triangledown}{\tau}_{ij}$.

The total strain measure ϵ_{ij} is calculated in a manner consistent with the integration of D_{ij}. This generates logarithmic strain measures which are energy conjugate to the Kirchoff stress τ_{ij} which, as discussed above, is approximately equal to the Cauchy stress σ_{ij} in the analyses under consideration.

END

DATE

FILMED

3 - 88

DTIC